A compact UWB MIMO antenna augmented with isolation improvement structures *in situ* with ground stubs and slots

Jeet Banerjee[1] (ID), Abhik Gorai[2] (ID) and Rowdra Ghatak[3]

[1]Department of Electrical & Electronics Engineering, School of Engineering and Technology, Adamas University, Kolkata, West Bengal, India; [2]School of Electronics Engineering, KIIT Deemed University, Bhubaneswar, India and [3]Microwave and Antenna Research Laboratory, ECE Department, National Institute of Technology Durgapur, Durgapur, West Bengal, India

CAMBRIDGE
UNIVERSITY PRESS

Abstract

An orthogonally oriented microstrip-fed bi-element ultra-wideband (UWB) diversity antenna possessing a super-wide bandwidth, high isolation, and band rejection attributes is proposed. The intended diversity antenna uses a 2nd-order Cayley fractal tree-shaped neutralization line among a pair of radiating square monopoles along with additional components like extended ground stubs, hybrid Koch fractal parasitic elements, and an *L*-shaped defected ground structure to attain high isolation of < -20 dB over 3.1–18 GHz. To nullify the intervention from the existent wireless local area network band, a hybrid Koch–Minkowski slot is carved out from the radiators. A minimal inter-element spacing of 8 mm is attained with the suggested layout measuring 28 mm $(L) \times 42$ mm (W) in extent. The numerical as well as experimental investigations of vital diversity attributes like the envelope correlation coefficient, mean effective gain, total active reflection coefficient, and multiplexing efficiency depict high diversity actualization. The consistency amidst the simulation as well as the empirical results recommends the worthiness of the intended antenna for handy UWB and UWB multiple-input multiple-output systems.

Introduction

The attainment of extreme data rates using single-input single-output wireless structures is possible by increasing the transmission bandwidth or power [1]. Considering the biological threats within the indoor environment, the transmission power is restricted to 1 W [2]. The multiple-input multiple-output (MIMO) systems can overcome these constraints. In this situation, the design of MIMO radiators ensuring low mutual pairing is the prime design challenge [3]. Since the release of ultra-wide bandwidth via the Federal Communication Commission in 2002, the wireless realm has seen the hasty evolution of recent wireless technologies involving ultra-wideband (UWB) MIMO techniques [4].

However, during the implementation of compact UWB MIMO antennas in portable gadgets, it is testing to realize peak isolation among the radiators due to the negligible inter-element spacing. Hence, the improvement of isolation over a super-wide bandwidth becomes the vital design challenge [5]. A large variety of UWB MIMO radiators and distinctive decoupling strategies to limit mutual pairing amid closely placed elements has been manifested [6]. The decoupling methods are broadly sorted out into seven extensive classes, that are particularly the utilization of decoupling networks [7], engraved parasitic components [8], complementary split-ring resonators [9], electromagnetic bandgap constructions [10], defected ground formations [11], polarization diversity [12, 13], and neutralization lines (NLs) [14]. Some significant contributions utilizing NLs for isolation improvements are discussed subsequently.

A compact assembly of a pair of short-circuited monopoles and an NL to yield isolation improvement for USB dongle applications is described in paper [15]. The design suggested in paper [16] uses the combination of defected ground structure along with NL to realize a towering isolation of < -17 dB (ranging from 2.4 to 4.2 GHz) among two half-moon-shaped printed monopoles. Next, a dual-antenna system (covering 1.67–2.76 GHz) with F-shaped monopoles, ground branches, and NL is studied in paper [17]. The use of NL in this layout specifically aids to reduce mutual pairing at the lower edges of the operational bandwidth (1.7–2 GHz). The MIMO antenna investigated in paper [18] uses three NL to curtail pairing between 1.6 and 2.8 GHz. It also mentions the change of impedance facets of the antenna with the incorporation of multiple NLs. The proposed layouts in papers [19, 20] incorporate a U-framed NL and a pair of crossed NLs respectively for gaining isolation enhancement between radiating elements. The current literature (reported in papers [15–20]) lacks the exploration of a single NL to provide peak detachment in the undivided UWB extent (3.1–10.6 GHz) and the use of NLs in a UWB MIMO antenna

with polarization diversity. The use of fractal geometry for design-ing the decoupling structure provides miniaturization to the decoupling structure and the antenna. The use of fractal-based miniaturization techniques demands further exploration in UWB MIMO antennas utilizing NLs. The correlation between the offered radiators and alternative UWB diversity radiators produced within the recent works signifies various important features of the proposed methodology. The crucial among them are as follows:

1. The layout explores polarization diversity as suggested by paper [19] to attain a better impedance bandwidth. The proposed layout uses a fractal NL to provide miniaturization of the decoupling structure. The monopole elements are placed within a nominal inter-element spacing of $0.08\lambda_0$ (at 3 GHz) with common shared ground plane. Unlike papers [20, 21] and [18], where a single NL was unable to compensate for a wide frequency band, the recommended layout uses a single fractal NL to attain isolation improvement over a much wider bandwidth. The NL not only reduces the mutual coupling at the lower frequency band (between 3 and 8 GHz) but also does not affect the low mutual coupling at the higher frequency band (8–15 GHz).

2. The published literature indicates that the NL approach has been sufficiently explored to provide isolation enhancement in the lower frequencies ranging up to 3000 MHz. But, the standard literature lacks, the exploration of NL for attaining wideband isolation enhancement for the UWB spectrum. The proposed antenna explores a simple Cayley fractal tree-shaped NL to provide wideband isolation enhancement (3–7 GHz by more than 5 dB) and impedance bandwidth improvements (between 5 and 7 GHz as well as between 9 and 18 GHz).

3. The hybrid-Koch fractal parasitic elements improve impedance matching (3–5 GHz) as well as improve the isolation (between 3.3 and 11.5 GHz and between 13 and 18 GHz). The use of hybrid fractal geometry for designing the parasitic elements provides miniaturization of the isolation improvement and impedance matching structures.

4. The introduction of the hybrid fractal slots on the radiating monopoles leads to band rejection attributes at the wireless local area network (WLAN) (5.5 GHz) frequencies and leads to overall miniaturization of the band refusal designs.

5. The suggested antenna with space diversity is found to be compact and simple as compared to the designs reported in papers [16, 22–34]. An extensive study of existing literature on UWB diversity antenna indicates that the present radiator is the only design to attain isolation improvement through the whole UWB and super-wideband spectrum utilizing a single and simple fractal NL.

The paper is organized into four sections. Antenna design methodology presents the design methodology of the single-element as well as the two-element MIMO antenna with relevance of each design element and their detailed analysis utilizing the S-parameters along with the the surface current distributions. The results and associated discussions along with the analysis of the diversity parameters as well as the comparison with the existing literature on UWB MIMO antennas are discussed in the results and discussion section. The final section of the paper highlights the general conclusions and applications of the proposed design.
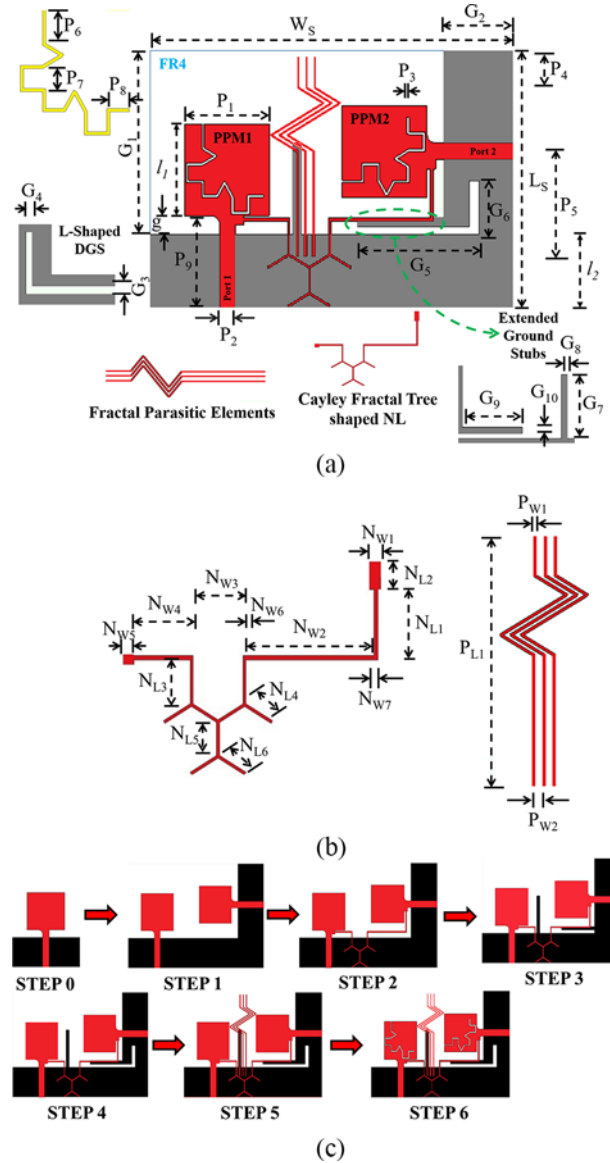

Figure 1. The optimized configuration of the suggested radiator. (a) Front view (the radiator is oriented along the *y–z* plane), (b) the Cayley fractal tree-shaped NL and the hybrid Koch fractal inspired parasitic elements, and (c) sequential steps of antenna design.

$L_S = 28$, $W_S = 42$, $G_1 = 20$, $G_2 = 8$, $G_3 = 0.8$, $G_4 = 0.2$, $G_5 = 14.02$, $G_6 = 5.8$, $G_7 = G_9 = 10$, $G_8 = G_{10} = 1$, $P_1 = 9.8$, $P_2 = 2.8$, $P_3 = 0.25$, $P_4 = 3.35$, $P_5 = 11.49$, $P_6 = 2.61$, $P_7 = 1.59$, $P_8 = 1.84$, $P_9 = 10$, $P_{L1} = 21.75$, $P_{W1} = 0.25$, $P_{W2} = 0.7$, $g = 2$, $N_{L1} = 5.7$, $N_{L2} = 1$, $N_{L3} = 3.58$, $N_{L4} = 2.72$, $N_{L5} = 2.68$, $N_{L6} = 2.72$, $N_{W1} = 1$, $N_{W2} = 11.72$, $N_{W3} = 4.5$, $N_{W4} = 5.27$, $N_{W5} = 1$, $N_{W6} = 0.25$, $N_{W7} = 0.35$.

Antenna design methodology

The recommended radiator is modeled and optimized employing the commercially available electromagnetic (EM) modeling computer application CST Microwave Studio™. The radiator is materialized over a low-cost FR4 material of depth 1.6 mm. The recommended radiator is depicted in Fig. 1(a) as well as 1(b). Fig. 1(c) presents the sequential stages of antenna evolution. For attaining simplicity of design as well as wide impedance bandwidth we select square-shaped radiators printed planar monopole 1 (PPM1) and printed planar monopole 2 (PPM2) as planar monopole elements
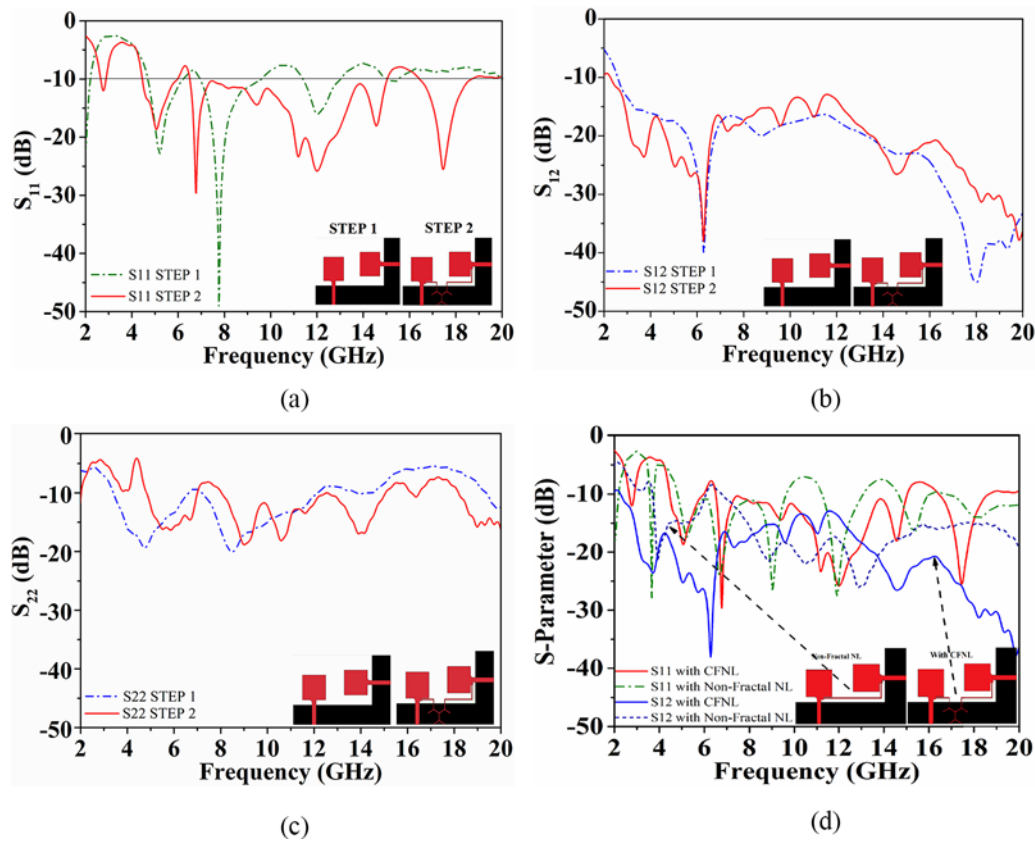
Figure 2. Analysis of S-parameter with an application of CFNL. (a) Comparison of S11, (b) S12, and (c) S22 after the application of CFNL and (d) comparison between application of fractal and non-fractal NL for impedance matching and isolation improvement.

[35] fed by microstrip feed via ports 1 and 2 respectively. For estimating the fundamental frequency of a square monopole radiator, we employ [36]

$$f_r = \frac{144}{l_1 + l_2 + g + \frac{A_1}{2\pi l_1 \sqrt{\varepsilon_{re}}} + \frac{A_2}{2\pi l_2 \sqrt{\varepsilon_{re}}}}. \quad (1)$$

Here, l_1 and l_2 indicate the stretch of ground structure and the radiating monopole, respectively; g indicates the split among the monopole and the ground plane; A_1 and A_2 indicate the area of the ground structure and the radiator, respectively (all dimensions in mm). ε_r is the effective dielectric constant identified as $\varepsilon_{re} = (\varepsilon_r + 1)/2$. The fundamental square-shaped monopole antenna is depicted in Fig. 1(c).

Realization of the diversity configuration

The diversity configuration as depicted in Fig. 1(c) is attained by an orthogonal combination of PPM1 and PPM2 maintaining a compact inert-element separation of 8 mm ($0.13\lambda_0$ at 3.1 GHz). The mutually perpendicular location of radiating monopoles is chosen to acquire high non-pairing as a result of polarization diversity. The individual monopoles are fed by a $P_2 \times P_9$ 50 Ω microstrip line. PPM1 and PPM2 have a common rectangular ground plane with identical width of G_2 but dissimilar lengths of W_S and L_S, respectively, and are placed behind the substrate. For attaining higher impedance matching (in terms of S_{22}) near the lower (3.8 GHz) and upper edges (9–18 GHz) of the UWB spectrum, an L-shaped

slot with a dimension of $G_5 \times G_3$ and $G_4 \times G_6$ is carved from the top of the common ground structure. To attain wideband impedance matching as well as high and wideband isolation amidst the radiating monopoles, a couple of rectangular extended ground stubs of identical dimensions is deployed as shown in Fig. 1(a). Stub 1 is positioned side by side with PPM1 and the 2nd stub is positioned side by side in the company of PPM2. The optimized extent of the UWB diversity radiator is given in Fig. 1.

Effects of introducing Cayley tree fractal NL

To attain bandwidth enhancement (by constructing a substitutive resonance near 3.8 GHz), additional decoupling (between 3 and 7 GHz by more than 5 dB), and impedance matching (between 9 and 18 GHz), a Cayley fractal neutralization line (CFNL) is connected to the peak impedance zone of the radiating monopole (near the excitation zone of the monopoles) as presented in Fig. 1(a) and (c) [18]. Fig. 2(a), (b), and (c) depict the improvement of S_{11}, S_{12}, and S_{22} with the introduction of the CFNL respectively.

The length of the NL is initiated at $0.5\lambda_0$ at 3.1 GHz (lowest resonant frequency) and is gradually tuned to obtain an optimum level of impedance matching as well as isolation [37]. The value of λ_0 at 3.1 GHz = 96.8 mm and the overall length of the CFNL is measured to be 50.7 mm. The theoretical and actual measure of the length of the fractal NL are in close agreement and thus justify the design methodology. According to paper [18], the suspended link acts as a NL by providing a counter-phase current to counter the original coupling current. Besides, the inductive and capacitive behaviors
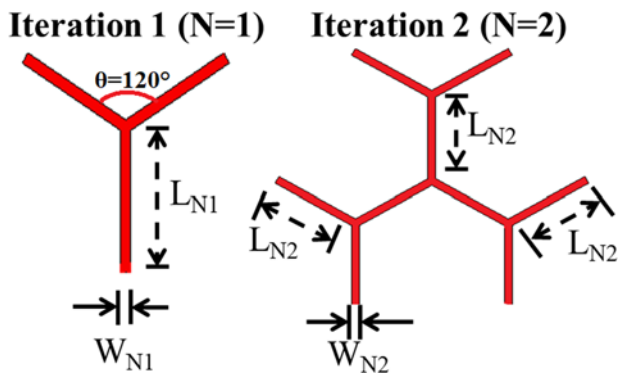
Figure 3. First two iterations (*N*) of the Cayley tree fractal curves. $L_{N1} = 5.36$ mm, $W_{N1} = W_{N2} = 0.25$ mm, $L_{N2} = 2.68$ mm.

Figure 4. The surface current spread over the radiator at (a) 4.3 GHz without the ground stubs, (b) 4.3 GHz with ground stubs, (c) 13.1 GHz without extended ground stubs, and (d) at 13.1 GHz with extended ground stubs.

of the NL are specified by its length and width, respectively. The NL is used to connect both monopoles close to their feeding to draw maximum current. The simple 2nd-order Cayley fractal tree geometry is chosen for designing the NL to reduce the design complexity and ease the realization as well as manufacturing process. This process of isolation improvement utilizing NL does not eliminate the basic pairing among the radiators, nevertheless improves the inter-port non-pairing [17].

The Cayley tree fractal-inspired NL is a *Y*-formed assembly (the 1st-order fractal, *N* = 1, Fig. 3) of three microstrip-line branches spaced apart from each other by 120° rotation angle. The length and breadth of an individual branch are uniform, i.e., $L_{N1} = 5.36$ mm and $W_{N1} = W_{N2} = 0.25$ mm, respectively. The fractal NL formation is proportionate across the *y*–*z* plane. The construction of the Cayley tree is by straightforward iterative function. The geometry is generated from an equilateral *Y* shape. Upon each iteration, two new branches are added to each terminal branch. The angle between each branch is kept constant (at $\theta = 120°$), maintaining a threefold rotational symmetry [38]. The number of tips in a Cayley tree of order $N = 3 \times 2^{N-1}$. The Cayley tree is a kind of dendrimer, also known as Bethe lattice. The construction procedure of the Cayley tree ($C_{s,t}$) ($s \geq 3, t \geq 0$) consists of *t* iterations. *S* is the number of nodes in the 1st iteration. $C_{s,0}$, for $t = 0$, consists of only a central vertex. For $t > 1$, the Cayley tree $C_{s,t}$ is obtained from $C_{s,t-1}$. In $C_{s,t}$, the pendent vertices are $s(s-1)^{n-1}$ and the *s*-degree vertices are [39]:

$$2\sum_{i=1}^{t}(s-1)^{i-1} - (s-1)^{n-1}. \tag{2}$$

The cardinality of vertex and edges in $C_{s,t}$ is

$$2\sum_{i=1}^{t}(s-1)^{i-1} + (s-1)^{t} \text{ and } s\sum_{i=1}^{t}(s-1)^{i-1} \tag{3}$$

respectively [39]. To attain miniaturization of the isolation improvement structure and to strengthen the despairing of the MIMO system with increasing iterations, a fractal-shaped NL is introduced in this layout. On top of each repetition, a pair of additional arms is added per terminating branch. The angle among every branch and the branch widths are identical to that of level 1 but the length of the arms (for $N = 2$) is shortened equally to $N_{L6} = 2.68$ mm. The overall length of the CFNL is found to be $\approx \lambda_0/2$ at 3.1 GHz. The use of 2nd-order Cayley tree fractal geometry for designing the NL aids to escalate the effective electrical path length, thereby allowing the monopole to resonate at
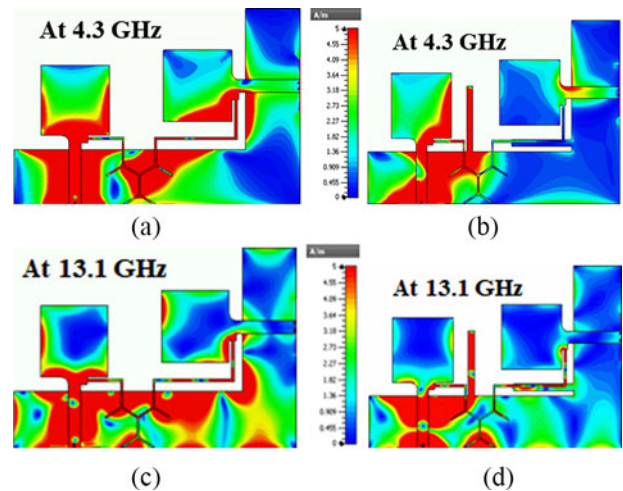
a low frequency of 3.8 GHz (see Fig. 2(a)). The incorporation of the CFNL improves the decoupling level drastically (by a minimum enhancement of 5 dB) between 3 and 7 GHz (see Fig. 2(b)). Figure 2(c) shows the improvement of S22 (among 10–20 GHz). Consequently, a wideband isolation enhancement can be attained due to modification in the surface current spread on the radiating monopoles, leading to modification in the impedance properties of the antenna [17]. It is evident from Fig. 2(d) that as compared to the non-fractal counterpart, the 2nd-order CFNL provides a higher isolation enhancement (between 3 and 8 GHz). Thus, the CFNL aids to improve both the impedance matching and the non-pairing among PPM1 and PPM2. It was also observed that with the increase in iterations of the CFNL, the isolation among the radiating elements increases as well as the complexity of the design also increases. To attain minimum design complexity, we orderly inspect elementary branching fractal formation, the Cayley tree.

Effects of introducing ground stubs and L-shaped defect in common ground plane

It was noticed from Fig. 4(a) and (b) that high currents move among the pair of monopole elements via the common ground plane. Also, the currents along the shared ground structure pass straight to port 2 through the ground corner. It is evident from Fig. 4(a) and (b) that the extended ground stubs are behaving as a reflector to minimize EM pairing [32]. The ground stubs can minimize the current over the ground structure moving among the PPM1 and PPM2. To examine the outcome of a pair of ground stubs on the scattering performance of the MIMO antenna, the simulated S_{11}, S_{21}, and S_{22} with and without the presence of stubs are plotted in Fig. 5(a) and (b) respectively. It is noticed from Fig. 5(a) and (b) that the inception of the ground stubs enhances the impedance bandwidth of the antenna in terms of S_{11} between 3.8 and 5 GHz and in terms of S_{22} between 3.8 and 7 GHz as well as between 12.6 and 18 GHz respectively. The addition of the ground stubs also strengthen the isolation (S_{12}/S_{21}) between 4.3 and 7 GHz as well as between 11 and 16.7 GHz. So, it can be concluded that in agreement with paper [27], the extended ground stubs improve both impedances matching as well as isolation of the
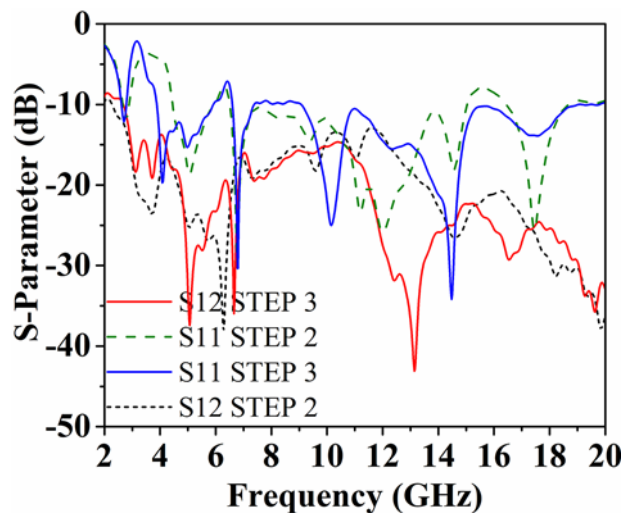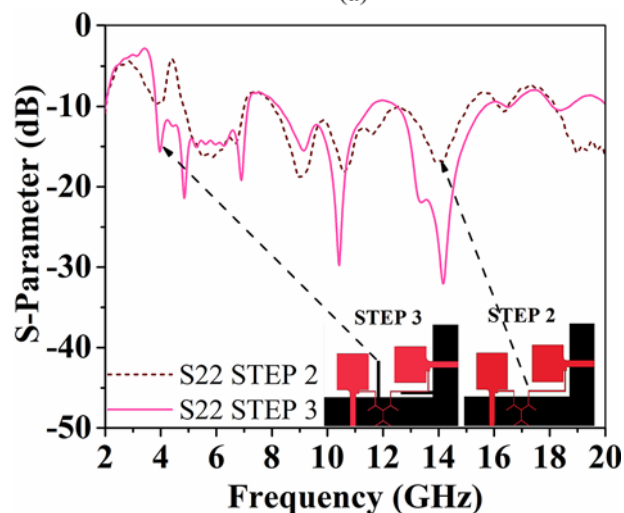
Figure 5. Scattering parameters of the radiator in the presence and absence of the extended ground stubs. (a) Comparison among S11 and S12 for STEP 2 and 3 and (b) comparison among S22 for STEP 2 and STEP 3.

Figure 6. The surface current spread over the radiator at (a) 3.7 GHz without the L-shaped slot, (b) 3.7 GHz with the L-shaped slot, and (c) comparison of S_{22} with and without the L-slot up on the ground structure.

diversity system. Next, an L-shaped slot is created by utilizing the corner of the common ground structure and the extended ground stub (as depicted in Fig. 1 [STEP 4]). Due to the elongation of the effective path length of the induced current (as depicted in Fig. 6(a)) on the ground structure [16], the impedance traits (S_{22}) of the radiator are modified, thereby allowing the radiator to possess a lower S_{22} cutoff frequency of 3.3 GHz instead of 3.9 GHz. A significant improvement of the S_{22} (especially near 3.5 GHz, 9 GHz, and 12–18 GHz) is noticed (see Fig. 6(b)). The parametric investigations have shown the negligible influence of the L-slot on the S_{11} and S_{12} characteristics of the antenna.

Introduction of hybrid fractal parasitic elements for isolation enhancements

A set of three hybrids (Koch–Koch) fractal parasitic elements are introduced among the radiating monopoles to attain wideband isolation enhancement (between the lower 2.7–4.7 GHz and the
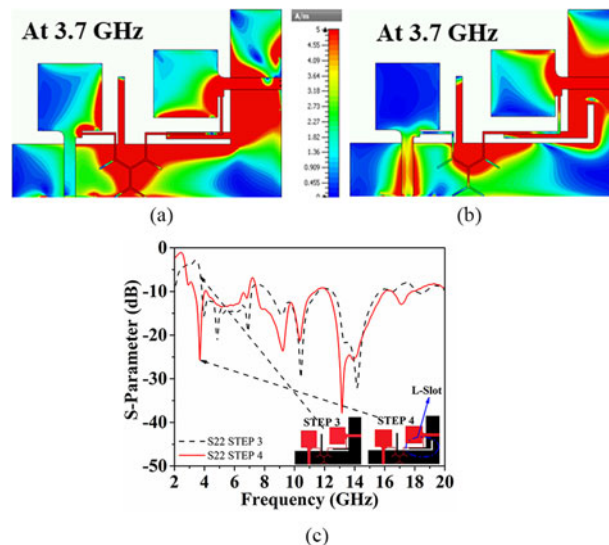
upper 7–16.7 GHz bands) as depicted in Fig. 7a. The hybrid fractal parasitic strips artificially produce a reverse field linking trace to nullify the primary field linking thereby enhancing isolation among the radiating monopoles [40]. The use of fractal parasitic elements provides better isolation (S_{12}/S_{21}) enhancement between 3.3 and 4.7 GHz as well as between 5.9 and 11.5 GHz and among 12.7 and 18 GHz as compared to non-fractal counterparts (see Fig. 7(b)). The length, position, and separation among the three parasitic elements are optimized by a series of parametric studies. Figure 7(c) indicates that the introduction of hybrid fractal parasitic elements allows the antenna to resonate near 3.1 GHz, thereby covering the complete UWB bandwidth. The use of fractal geometry for designing the parasitic elements provides miniaturization of the isolation improvement and impedance matching structures [40].

Band rejection using hybrid fractal slots

A pair of hybrids (Koch–Minkowski) fractal slots (as shown in Fig. 8(a) and (b)) is carved out from PPM1 and PPM2 for attaining band rejection characteristics across the WLAN band (5.15–5.825 GHz). Minkowski along with Koch's fractal geometries are used as generator curves to obtain the final structure, which contains the 14 segments. The resonant frequency of the band notch slot can be evaluated by using Equation (4):

$$f_{notch} = \frac{c}{2L_{Total}\sqrt{\varepsilon_{eff}}}. \qquad (4)$$

Here, c stands for the speed of light across empty space, L_{Total} stands for the gross extent of the slot, with $\varepsilon_{eff} = \varepsilon_r + 1/2$. The overall stretch of the hybrid fractal opening is found to be $\approx \lambda_0/2$ (along 5.5 GHz). The radiator's S-parameter post-insertion of the hybrid fractal slots is depicted by Fig. 8(a) and (b). The hybrid
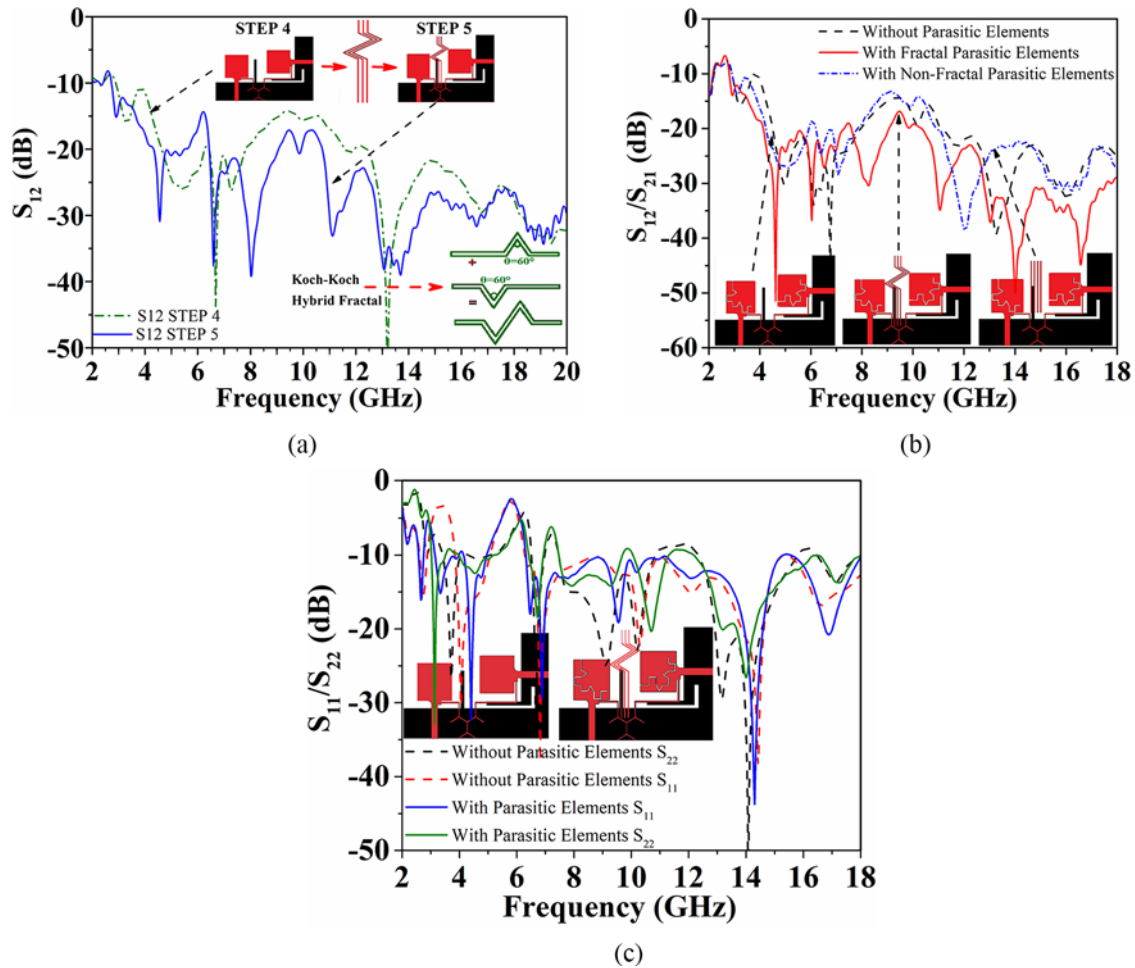
Figure 7. Improvement of isolation (a) with the addition of hybrid (Koch–Koch) fractal parasitic elements, (b) comparison of isolation improvement in the absence of parasitic elements, by non-fractal, and hybrid fractal counterparts respectively, along with the (c) comparison of S_{11} and S_{22} characteristics with and without parasitic elements.
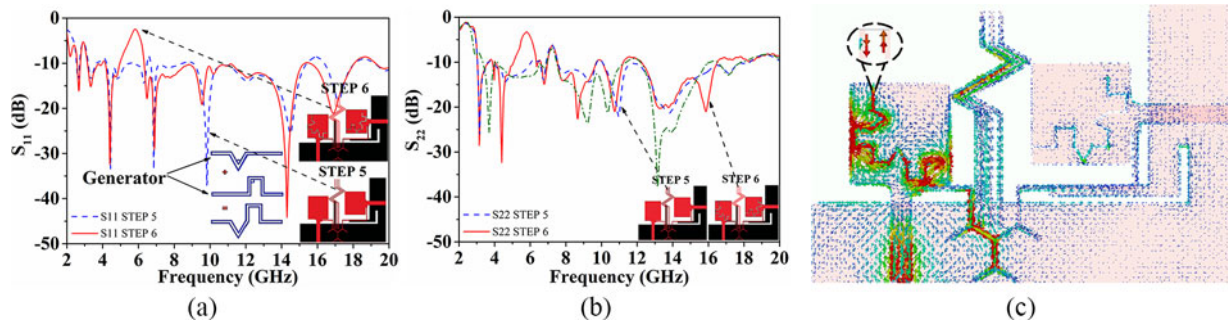

Figure 8. Comparison of (a) S_{11}, (b) S_{22} with the introduction of the hybrid fractal slots, and (c) oppositely directed surface currents on either wall of the hybrid fractal slot (at 5.5 GHz).

fractal slot behaves like an inductor and a capacitor in series with the antenna and causes refusal in the WLAN band [41]. Additionally, the current distribution shown in Fig. 8(c) suggests that the current in either wall of the hybrid fractal slot is oppositely directed. So current in one wall cancels the current in the other wall and thus provides band stop attributes. The parametric variations in the background have depicted that the stretch, breadth, and location of the slots are vital parameters in tuning the band rejection at the WLAN band.

Results and discussions

Impedance aspects and radiation performance

The realized archetype for the recommended diversity radiator is shown in the inset of Fig. 9(b) along with its S-parameters validated by employing Rhode and Schwarz ZVA 40 VNA. Figure 9(a), as well as Fig. 9(b), illustrates that the measured functional bandwidth stretches from 3 to 18 GHz ($S_{11} \leq -10$ dB) and $S_{22} \leq -10$ dB (covering a super-wide bandwidth including the UWB spectrum) sharply
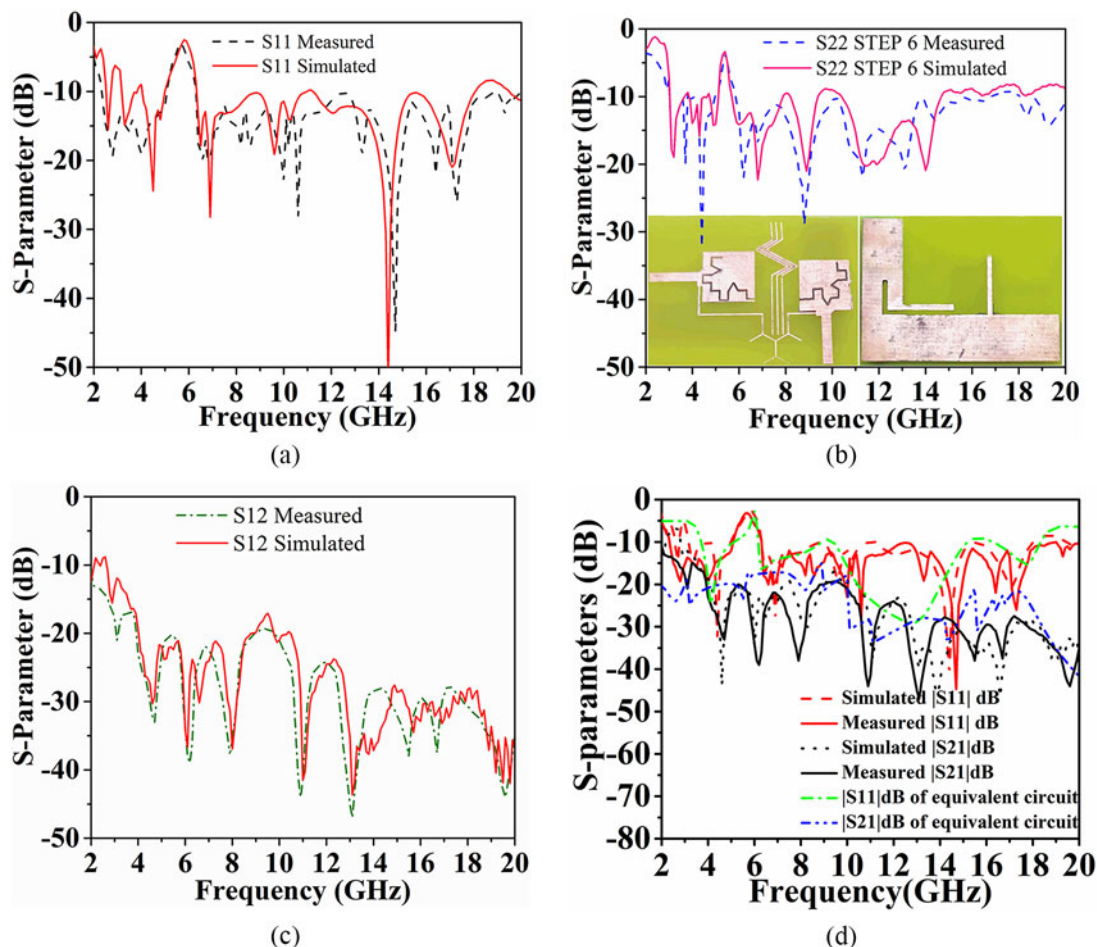
Figure 9. Numerical as well as empirical (a) S_{11}, (b) S_{22} (inset realized antenna), (c) S_{12}, and (d) S-parameters from equivalent circuit model.
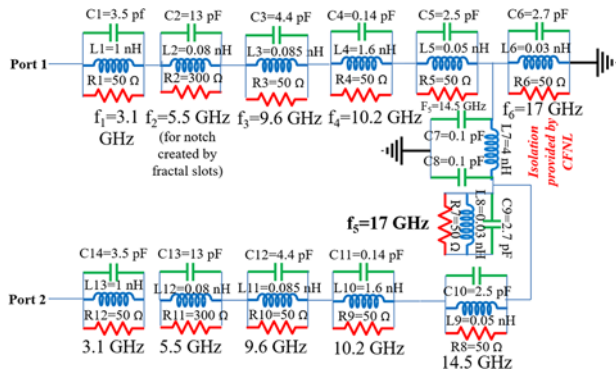

Figure 10. Equivalent circuit of the proposed antenna.

excluding a pre-assigned narrow band among 5.15–5.825 GHz (WLAN). Figure 9(c) depicts that the $|S_{21}|$ is below −20dB between 4 and 18 GHz showing high and wideband isolation. However, the $|S_{12}|$ is found to attain lesser values (between −13 and −18 dB) between 3.1 and 4 GHz. Figure 9(d) depicts the comparison between the S-parameters received by simulation, empirical, and equivalent circuit (the circuit is depicted in Fig. 10) investigations of the suggested antenna. Figure 9 shows a good accord between the simulation and the empirical results. Some variations amidst the

numerical as well as the experimental results are noticed because of variabilities of dielectric constant and loss tangent of the substrate. Figure 10 illustrates the equivalent circuit setup drawn out for the suggested super-wideband diversity antenna. The equivalent circuit is modeled by analyzing the S-parameter of the suggested antenna. The parallel resonant circuit at 3.1 GHz is modeled by employing *L1, C1*, and *R1*. The second resonance frequency is specified by implementing *L3, C3*, and *R3* in the form of a parallel resonant circuit. Likewise, the third resonant frequency (at 10.2 GHz) is configured by utilizing *L4, C4*, and *R4*. The fourth resonant frequency is modeled by a parallel resonant circuit *C5, L5*, and *R5*. The fifth resonant frequency at 17 GHz is modeled by using *C6, L6*, and *R6*. It is evident from Fig. 9(d) that a band refusal is extended at 5.5 GHz. This observation suggests that the band refusal trait at 5.5 GHz (due to the hybrid fractal slots) could be configured by utilizing a parallel resonant circuitry comprising *L2, R2*, and *C2*. The isolation improvement provided by the CFNL is modeled by utilizing a *T*-network of *L7, C7*, and *C8*.

Figure 11 portrays the normalized numerical and empirical two-dimensional radiation patterns of the recommended radiator. The two-dimensional radiation pattern for each antenna element is examined along with two sets of planes (the *X–Z* plane together with the *X–Y* plane). The examination is executed for three sets of frequency bands located at 3.3 GHz, 7 GHz, and 15 GHz. During the evaluation, port 1 is solely excited, during that time the second
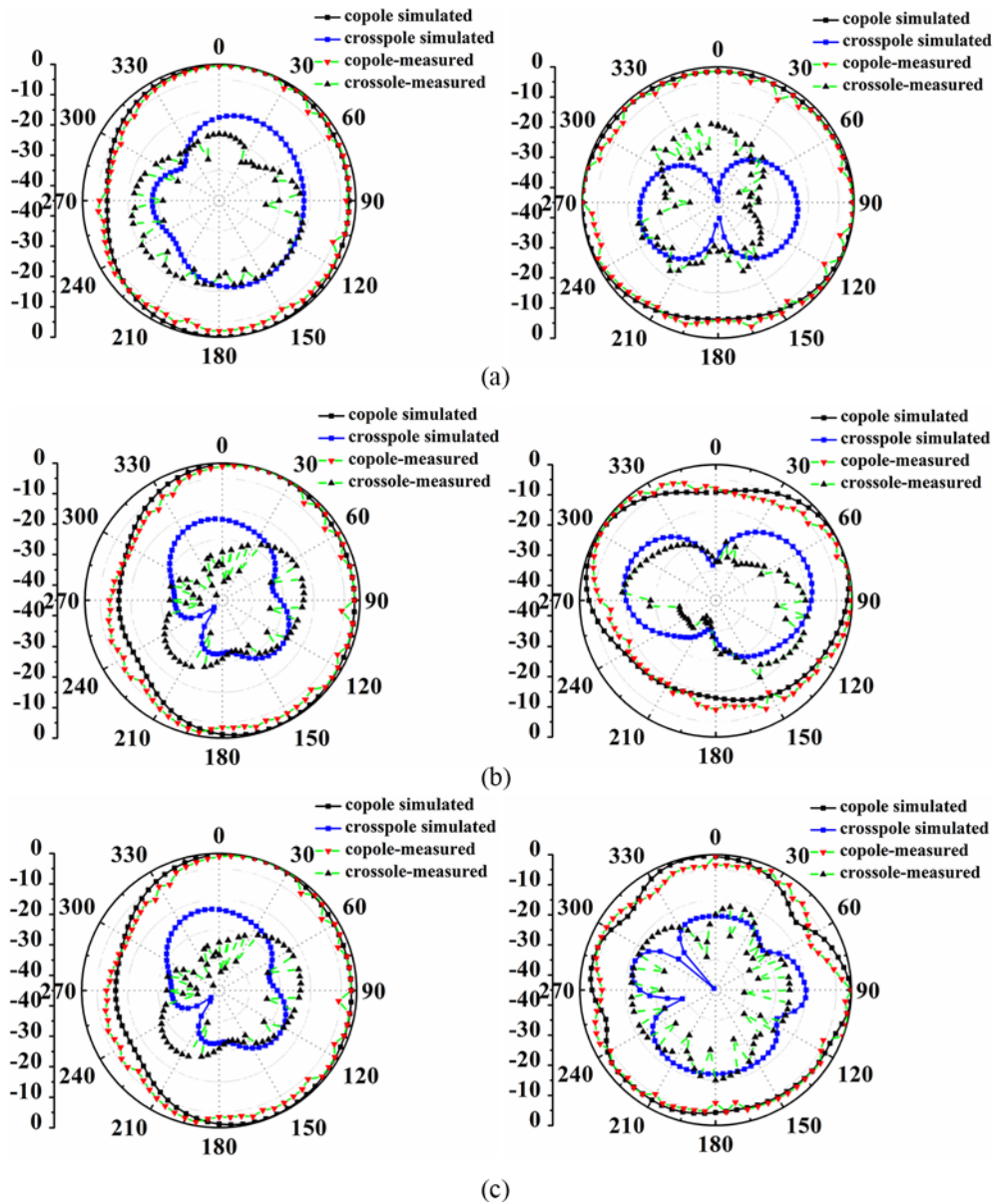
Figure 11. Radiation patterns of the suggested super-wideband diversity radiator (with the radiator aligned in the *y–z* plane) at (a) 3.3 GHz, (b) 7 GHz, and (c) 15 GHz.

port is discontinued employing a 50 Ω load. Figure 11(a)–(c) reveal that the two-dimensional radiation patterns across the *X–Y* plane (*H*-plane) are low on directional radiation (at the bottom end of the UWB spectrum [at 3.3 GHz]) as compared to the patterns at the top verge (at 7 GHz). The patterns at the higher verge of the UWB are close to omnidirectional accompanying multiple lobes. Monopole-like patterns are noticed in the *X–Z* plane (*E*-plane). The nearing omnidirectionality of the radiation patterns across the *X–Y* plane ensures the enclosure of a uniform along with a broad range for utilization in the UWB system.

Next, Fig. 12 presents the maximum empirical gain along with the total radiation efficiency for the suggested radiator. The empirical gain is found to fluctuate between 1.06 and 5.1 dBi, excluding an elimination band centered at 5.5 GHz. The real radiation efficiency (empirical value) spans between 50 and 76%. Figure 12 also depicts a deep drop in realized gain (drops to −1.03 dBi) and efficiency (drops to 22.5%) at 5.5 GHz, providing firm evidence of effective interference suppression at WLAN frequencies.

For increasing the spectral efficiency of MIMO systems, spatial multiplexing is important [42]. A metric for estimating the diversity radiator's functioning in the form of spatial multiplexing is the multiplexing efficiency. A closed-form expression of multiplexing efficiency is reported in paper [40] and is given by Equation (5)

$$\eta_{MUX} = \sqrt{(1 - |\rho_C|^2)\eta_1\eta_2}. \tag{5}$$

Here, ρ_C represents the complex correlation coefficient amid a couple of monopoles, whereas envelope correlation coefficient (ECC) $\approx |\rho_C|^2$, as well as η_n, is the overall effectiveness for the *n*th radiator. The multiplexing efficiency of the recommended radiator and its likeness to the total efficiency plot can be observed from Fig. 12 across the intended UWB bandwidth, as a result of low ECC.
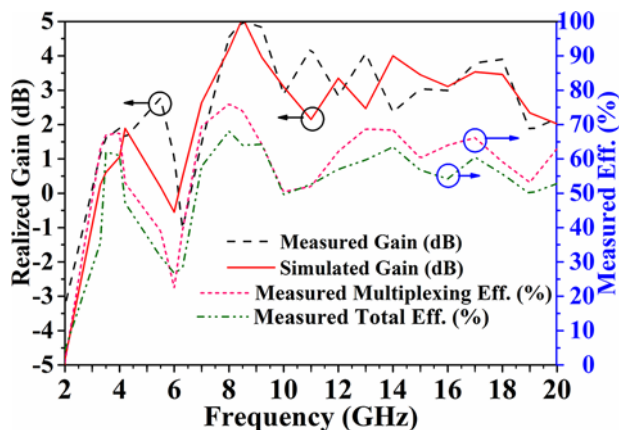
Figure 12. Simulated and measured realized gain as well as radiation efficiency of the suggested antenna.

Figure 13. Measured ECC and DG of the recommended antenna.

Diversity performance

To demonstrate the diversity features for the proposed diversity arrangement, the ECC is computed utilizing Equations (6) and (7) [42]. As Equation (7) takes into account both coupling from antenna ports as well as coupling due to the radiated fields, we use Equation (7) to compute the ECC. The far-field method of ECC measurement was utilized (i.e., Equation (7)) as the one reported using Equation (6) requires the antenna to be lossless and single-mode antenna [42]. For improving the reliability of detection (of the identical samples of individual information), the diversity gain (DG) is computed [42]. The DG is calculated using Equation (8), and individually these outcomes are plotted in Fig. 13:

$$\rho_e = \frac{\left| S_{11}^* S_{12} + S_{21}^* S_{22} \right|^2}{\sqrt{(1 - |S_{11}|^2 - |S_{21}|^2)(1 - |S_{22}|^2 - |S_{12}|^2)} \eta_{rad1} \eta_{rad2}} \quad (6)$$

$$\rho_e = \frac{\left| \iint [E_1(\theta, \varphi) * E_2(\theta, \varphi)] d\Omega^2 \right|}{\iint\limits_{4\pi} |E_1(\theta, \varphi)|^2 d\Omega \iint\limits_{4\pi} |E_2(\theta, \varphi)|^2 d\Omega} \quad (7)$$

$$DG = 10\sqrt{1 - |\rho_e|^2}. \quad (8)$$

The ECC value in Fig. 13 is found to be lower than the experimental margin of 0.5 [41], and the DG is found to be well above 9.5 dB, depicting desirable diversity characteristics.

Mean effective gain (MEG)

To inspect the influence of the surrounding on the radiation traits of the antenna as well as to determine the correlative mean power among the signals offered by the individual radiator, the MEG is employed. The MIMO realization along with the channel aspects of the radiator is bound to be high, if the proportion of MEG ($|MEG1/MEG2|$) of the pair of monopoles is under ± 3 dB [43]. The steadiness of MEG is noticeable in Fig. 14. It is also perceived that the proportion of MEG is well under the reasonable margin of ± 3 dB in the entire UWB bandwidth and beyond (up to 20 GHz).
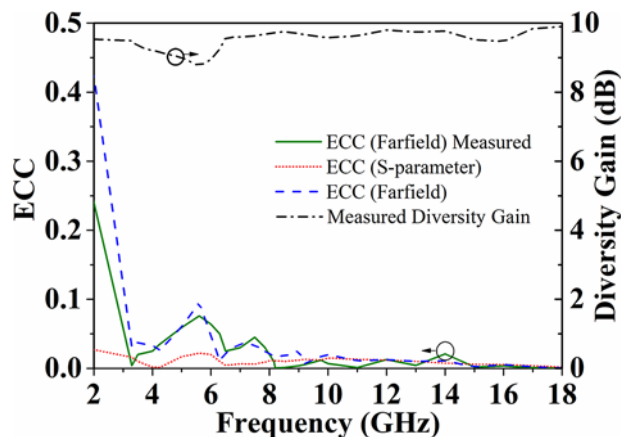
Total active reflection coefficient (TARC)

The S-parameter alone of a diversity system cannot be satisfactorily specified, the efficiency and bandwidth

$$TARC = \sqrt{\frac{(S_{11} + S_{12})^2 + (S_{21} + S_{22})^2}{2}}. \quad (9)$$

For the implicit estimation of a radiating system with diversity, the TARC is utilized. The investigation of the TARC also aids in examining the results of phase changes among the pair of ports on the resonance response of the radiator. The TARC of a bi-port diversity system [44] is discovered using Equation (9). The TARC for a diversity antenna system must be restricted to <0 dB [36]. Fig. 14b conveys that the recommended antenna manifests a TARC below −24.5 dB for the entire super-wide bandwidth (3.1–18 GHz).

A comparative study amid the recommended radiator and already proclaimed UWB MIMO radiators in papers [16, 22–34] is listed in Table 1. The analogy outlines the newness of the recommended radiator in comparison to the UWB diversity radiators reported in the recent past.

The design and investigation of super-wideband MIMO antennas with polarization diversity as well as common ground plane remains minimally explored in the reported literature and thus is a significant novelty of the suggested work. The suggested antenna is found to be smaller than all the antennas enlisted in the comparison Table 1 except paper [16]. The suggested antenna covers a much wider impedance bandwidth as compared to all the designs enlisted in Table 1. Additionally, the reported antenna covers the same impedance bandwidth (ranging from 3 to 18 GHz with an isolation of >20 dB) as suggested by paper [32] but is realized in a smaller footprint and has attained a larger peak gain. The wideband isolation as compared to paper [32] is realized with a comparatively lower inter-element spacing of 8 mm. The suggested radiator attains a higher realized gain as compared to the related works reported in Table 1, considering its realization over the low cost FR4 substrate.

Conclusion

The paper recommends a spatially diverse two-element super-wideband MIMO antenna separated by a minimal inter-element spacing of $0.08\lambda_0$ (at 3 GHz) and realized within a compact layout
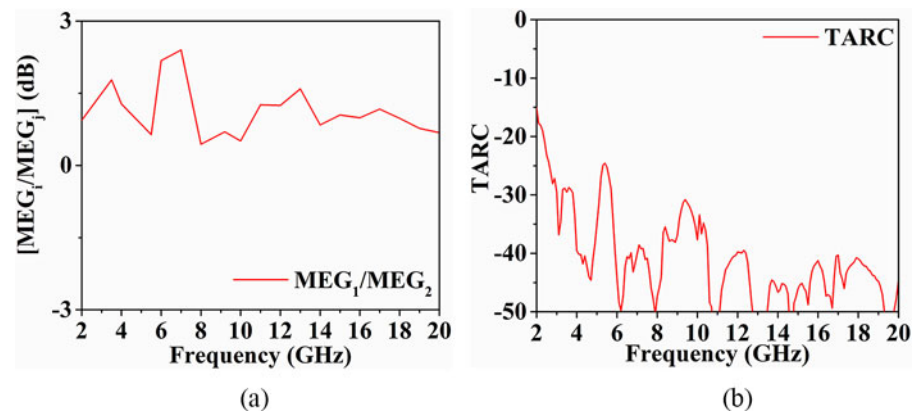
Figure 14. Measured (a) mean effective gain of the suggested antenna and (b) TARC.

Table 1. Comparison of the recommended antenna with formerly reported UWB MIMO antennas

Ref. No.	Size (mm × mm) and area (mm²)	Impedance bandwidth (GHz)	S12 (dB)	Real. gain (dB)	ECC	Substrate material
[22]	44 × 44 and 1936	2.95–10.8	>15.5	2.4–4	<0.04	FR4
[16]	32 × 36 and 1152	3–10	>20		<0.0025	FR4
[23]	38 × 38 and 1444	3–15	>20	0.5–5	<0.2	Neltec
[24]	50 × 80 and 4000	4.2–6.6	>17	5	0.06	Roger
[25]	50 × 40 and 2000	3.5–11	>20	2.35 (max.)	<0.02	FR4
[26]	35 × 40 and 1400	3.1–10.6	−16	3.1–6.2	<0.01	Taconic
[27]	30.5 × 47 and 1433.5	4.3–10.1	>16.8	0.9–3.84	<0.002	FR4
[28]	30 × 40 and 1200	2.4, 3.1–10.6	>15	-	<0.15	FR4
[29]	38.5 × 38.5 and 1482.3	3.08–11.8	>15	1.4–3.6	<0.02	FR4
[30]	38.3 × 38.3 and 1444	3–13.2	>17	4.1 (avg.)	<0.02	Taconic
[31]	80 × 35 and 2800	2.57–12.2	>13	3.5–5.8	<0.005	Teflon
[32]	40 × 40 and 1600	3–18	>20	1.5–4	<0.03	FR4
[33]	85 × 50 and 4250	2.0–9.50	>20	1.5	<0.03	FR4
[34]	41 × 99.4 and 4075.4	4.3–10.6	>15	<4.3	<0.007	FR4
This work	**42 × 28 and 1176**	**3.1–18**	**>20**	**1.06–5.1**	**<0.1**	**FR4**

of 42 × 28 mm². The amalgamation of the 2nd-order CFNL, a pair of extended ground stubs, and three hybrids (Koch–Koch) fractal parasitic strip results in mutual coupling lower than −20 dB between 3.1 and 18 GHz. The engravement of the hybrid fractal slots on the radiating microstrip-fed monopoles leads to band rejection in the WLAN band, thereby suppressing interference from narrowband wireless technologies. For attaining miniaturization of the band refusal and the isolation improvement structures, the fractal geometry is utilized. The suggested diversity antenna possesses a peak realized gain of 5.1 dB. The antenna exhibits a low ECC of <0.1 in the entire operating band. The proposed design has the inherent advantage of being integrated into portable UWB devices as well as is compatible with MIC/MMIC designs due to its simple design, compact size, fair gain considering its realization over low-cost FR4 substrate, and the possession of 60% clearance area behind the antenna as compared to competing 3D or multi-layered structures. The simulated $|S_{11}|$ dB, $|S_{22}|$, and $|S_{12}|$ dB are in agreement with the measurement results as well as those obtained from the equivalent circuit model of the proposed MIMO antenna. Satisfactory radiation and diversity characteristics of the proposed MIMO antenna are attained for portable wireless UWB MIMO applications.

Competing interests. The authors report no conflict of interest.

References

1. **Proakis JG** (2008) *Digital Communications*. New York: McGraw-Hill.
2. **Paulraj AJ, Gore DA, Nabar RU and Bolcskei H** (2004) An overview of MIMO communications – A key to gigabit wireless. *Proceedings of the IEEE* **92**(2), 198–218.
3. **Jensen MA and Wallace JW** (2004) A review of antennas and propagation for MIMO wireless communications. *IEEE Transactions on Antennas and Propagation* **52**(11), 2810–2824.
4. **Sharawi MS** (2017) Current misuses and future prospects for printed multiple-input, multiple-output antenna systems [wireless corner]. *IEEE Antennas and Propagation Magazine* **59**(2), 162–170.
5. **Liu L, Cheung SW and Yuk TI** (2013) Compact MIMO antenna for portable devices in UWB applications. *IEEE Transactions on Antennas and Propagation* **61**(8), 4257–4264.

6. **Malik J, Patnaik A and Machavaram K** (2018) *Compact Antennas for High Data Rate Communication: Ultra-Wideband (UWB) and Multiple-Input-Multiple-Output (MIMO) Technology*, Vol. 14. India: Springer International Publishing.

7. **Gorai A and Ghatak R** (2020) Utilization of Shorted Fractal Resonator topology for high isolation and ELC resonator for band suppression in compact MIMO UWB antenna. *International Journal of Electronics and Communications* **113**, 152978.

8. **Roshna TK, Deepak U, Sajitha VR, Vasudevan K and Mohanan P** (2015) A compact UWB MIMO antenna with reflector to enhance isolation. *IEEE Transactions on Antennas and Propagation* **63**(4), 1873–1877.

9. **Khan MS, Capobianco A-D, Asif SM, Anagnostou DE, Shubair RM and Braaten BD** (2017) A compact CSRR-enabled UWB diversity antenna. *IEEE Antennas and Wireless Propagation Letters* **16**, 808–812.

10. **Ghosh S, Tran T-N and Le-Ngoc T** (2014) Dual-layer EBG-based miniaturized multi-element antenna for MIMO systems. *IEEE Transactions on Antennas and Propagation* **62**(8), 3985–3997.

11. **Banerjee J, Karmakar A, Ghatak R and Ranjan Poddar D** (2017) Compact CPW-fed UWB MIMO antenna with a novel modified Minkowski fractal defected ground structure (DGS) for high isolation and triple band-notch characteristic. *Journal of Electromagnetic Waves and Applications* **31**(15), 1550–1565.

12. **Diallo A, Luxey C, Thuc PL, Staraj R and Kossiavas G** (2006) Study and reduction of the mutual coupling between two mobile phone PIFAs operating in the DCS 1800 and UMTS bands. *IEEE Transactions on Antennas and Propagation* **54**(11), 3063–3074.

13. **Ibrahim A, Eltokhy A and Daw A** (2023) Four ports MIMO printed antenna with high isolation for UWB and X-band systems. *International Journal of Microwave and Wireless Technologies* **15**(9), 1601–1609.

14. **Dharmarajan A, Kumar P and Afullo TJO** (2022) A high gain UWB human face shaped MIMO microstrip printed antenna with high isolation. *Multimedia Tools and Applications* **81**, 34849–34862.

15. **Su S, Lee C and Chang F** (2012) Printed MIMO-antenna system using neutralization-line technique for wireless USB-dongle applications. *IEEE Transactions on Antennas and Propagation* **60**(2), 456–463.

16. **See CH, Abd-Alhameed RA, Abidin ZZ, McEwan NJ and Excell PS** (2012) Wideband printed MIMO/diversity monopole antenna for WiFi/WiMAX applications. *IEEE Transactions on Antennas and Propagation* **60**(4), 2028–2035.

17. **Wang Y and Du Z** (2013) A wideband printed dual-antenna system with a novel neutralization line for mobile terminals. *IEEE Antennas and Wireless Propagation Letters* **12**, 1428–1431.

18. **Wang Y and Du Z** (2014) A wideband printed dual-antenna with three neutralization lines for mobile terminals. *IEEE Transactions on Antennas and Propagation* **62**(3), 1495–1500.

19. **Ban Y, Chen Z, Kang K and Li JL** (2014) Decoupled hepta-band antenna array for WWAN/LTE smartphone applications. *IEEE Antennas and Wireless Propagation Letters* **13**, 999–1002.

20. **Wang S and Du Z** (2015) Decoupled dual-antenna system using crossed neutralization lines for LTE/WWAN smartphone applications. *IEEE Antennas and Wireless Propagation Letters* **14**, 523–526.

21. **Cihangir A, Ferrero F, Jacquemod G, Brachat P and Luxey C** (2014) Neutralized coupling elements for MIMO operation in 4G mobile terminals. *IEEE Antennas and Wireless Propagation Letters* **13**, 141–144.

22. **Liu Y and Tu Z** (2017) Compact differential band-notched stepped-slot UWB-MIMO antenna with common-mode suppression. *IEEE Antennas and Wireless Propagation Letters* **16**, 593–596.

23. **Sipal D, Abegaonkar MP and Koul SK** (2017) Easily extendable compact planar UWB MIMO antenna array. *IEEE Antennas and Wireless Propagation Letters* **16**, 2328–2331.

24. **Jehangir SS and Sharawi MS** (2017) A miniaturized UWB biplanar Yagi-like MIMO antenna system. *IEEE Antennas and Wireless Propagation Letters* **16**, 2320–2323.

25. **Lin G, Sung C, Chen J and Houng M** (2017) Isolation improvement in UWB MIMO antenna system using carbon black film. *IEEE Antennas and Wireless Propagation Letters* **16**, 222–225.

26. **Zhang S, Ying Z, Xiong J and He S** (2009) Ultrawideband MIMO/diversity antennas with a tree-like structure to enhance wideband isolation. *IEEE Antennas and Wireless Propagation Letters* **8**, 1279–1282.

27. **Sohi AK and Kaur A** (2021) Computational analysis of a dual-port semi-circular patch antenna combined with Koch curve fractals for ultra-wideband systems. *Engineering Reports* **3**, 12378.

28. **Deng J-Y, Guo L-X and Liu X-L** (2016) An ultrawideband MIMO antenna with a high isolation. *IEEE Antennas and Wireless Propagation Letters* **15**, 182–185.

29. **Kang L, Li H, Wang X and Shi X** (2015) Compact offset microstrip-fed MIMO antenna for band-notched UWB applications. *IEEE Antennas and Wireless Propagation Letters* **14**, 1754–1757.

30. **Gómez-Villanueva R and Jardón-Aguilar H** (2019) Compact UWB uni-planar four-port MIMO antenna array with rejecting band. *IEEE Antennas and Wireless Propagation Letters* **18**(12), 2543–2547.

31. **Tang X, Yao Z, Li Y, Zong W, Liu G and Shan F** (2021) A high performance UWB MIMO antenna with defected ground structure and U-shape branches. *International Journal of RF and Microwave Computer-Aided Engineering* **31**, 22270.

32. **Tang Z, Zhan J, Wu X, Xi Z and Wu S** (2020) Simple ultra-wider-bandwidth MIMO antenna integrated by double decoupling branches and square-ring ground structure. *Microwave and Optical Technology Letters* **62**, 1259–1266.

33. **Zhao X, Yeo SP and Ong LC** (2018) Planar UWB MIMO antenna with pattern diversity and isolation improvement for mobile platform based on the theory of characteristic modes. *IEEE Transactions on Antennas and Propagation* **66**(1), 420–425.

34. **Sohi AK and Kaur AA** (2020) Complementary Sierpinski gasket fractal antenna array integrated with a complementary Archimedean defected ground structure for portable 4G/5G UWB MIMO communication devices. *Microwave and Optical Technology Letters* **62**, 2595–2605.

35. **Agrawall NP, Kumar G and Ray KP** (1998) Wide-band planar monopole antennas. *IEEE Transactions on Antennas and Propagation* **46**(2), 294–295.

36. **Thomas KG and Sreenivasan MA** (2010) Simple ultrawideband planar rectangular printed antenna with band dispensation. *IEEE Transactions on Antennas and Propagation* **58**(1), 27–34.

37. **Banerjee J, Gorai A and Ghatak R** (2022) A novel isolation improvement technique using fractal neutralization line with dual band rejection attributes in a compact UWB MIMO antenna. *International Journal of Microwave and Wireless Technologies* **15**, 1–12.

38. **Gottheim S, Zhang H, Govorov AO and Halas NJ** (2015) Fractal nanoparticle plasmonics: The Cayley tree. *ACS Nano* **9**(3), 3284–3292.

39. **Imran M, Baig AQ and Khalid W** (2018) On topological indices of fractal and Cayley tree type dendrimers. *Discrete Dynamics in Nature and Society* **2018**, 2684984.

40. **Banerjee J, Gorai A and Ghatak R** (2020) Design and analysis of a compact UWB MIMO antenna incorporating fractal inspired isolation improvement and band rejection structures. *AEU-International Journal of Electronics and Communications* **122**, 153274.

41. **Zheng Z, Chu Q and Tu Z** (2009) Compact band-rejected ultrawideband slot antennas inserting with λ/2 and λ/4 resonators. *IEEE Transactions on Antennas and Propagation* **59**(2), 390–397.

42. **Sharawi MS** (2013) Printed multi-band MIMO antenna systems and their performance metrics [wireless corner]. *IEEE Antennas and Propagation Magazine* **55**(5), 218–232.

43. **Gurjar R, Upadhyay DK, Kanaujia BK and Sharma K** (2019) A novel compact self-similar fractal UWB MIMO antenna. *International Journal of RF and Microwave Computer-Aided Engineering* **29**, 21632.

44. **Chae SH, Oh S-K and Park S-O** (2007) Analysis of mutual coupling, correlations, and TARC in WiBro MIMO array antenna. *IEEE Antennas and Wireless Propagation Letters* **6**, 122–125.

Jeet Banerjee received his B.Tech. and M.Tech. degrees in the years 2013 and 2015, respectively. Currently, he works as an Assistant Professor in the Department of Electrical and Electronics Engineering, Adamas University, Kolkata, West Bengal, India. Mr. Banerjee is parallel associated with the Department of ECE, National Institute of Technology Durgapur, India, as a Part-Time Research Scholar and is in the advanced stage of his Ph.D. studies. He has more than 20 publications in various international/national journals and conferences of repute. His primary research area lies in fractal UWB and UWB MIMO antenna design. He is the winner of the best paper award/outstanding paper award at four international/national conferences. He is also elected as the youngest executive council member of the Institution of Electronics and Telecommunication Engineers (IETE) Kolkata center via state-wide elections for the term 2022–2024.

Abhik Gorai received his M.Tech. and Ph.D. degrees in the years 2013 and 2020, respectively, from National Institute of Technology, Durgapur, India. He served in Huawei Telecommunication and Alcatel Lucent after his B.Tech. Currently, he is an Assistant Professor in Kalinga Institute of Industrial Technology. His primary research interests include fractal UWB antenna, metasurface, metamaterials, and substrate integrated waveguide-based antenna and filter design.

Rowdra Ghatak initiated his career in microwave engineering as a trainee with the CEERI Pilani, Pilani, India, in the domain of fabrication and testing of S-band magnetrons. Thereafter, he served at the National Institute of Science and Technology, Berhampur, and The University of Burdwan. He is currently a Professor with the Electronics and Communication Engineering Department, National Institute of Technology Durgapur, Durgapur, India. He has more than 250 publications in various national/international journals and conferences. His research interests include in the areas of fractal antenna, metamaterials, application of evolutionary algorithms to electromagnetic optimization problems, RFID, and computational electromagnetic and microwave passive and active circuit design. Dr. Ghatak was a recipient of the URSI Young Scientist Award in 2005. He also received support under the DST Young Scientist scheme for the development of UWB radiating systems for imaging RADAR. He has served in various selection as well as project review committees in the State as well as in the National domain. He has also served as a reviewer for a NPTEL course on antennas. He is a member of the board of studies at UG and PG levels at various state and central universities. He is also serving as a Research Advisor to the TCS Research in the domain of mmWave radio design and radiating system, and his current research interests include linear and nonlinear CAD techniques and low-noise receivers.